Available online at www.sciencedirect.com

ScienceDirect

Acta Materialia 89 (2015) 268–277

Acta MATERIALIA

www.elsevier.com/locate/actamat

Microstructural characteristics and elastic modulus of porous solids

Zhangwei Chen,* Xin Wang, Finn Giuliani and Alan Atkinson

Department of Materials, Imperial College London, London SW7 2AZ, United Kingdom

Received 23 November 2014; revised 8 February 2015; accepted 9 February 2015
Available online 26 February 2015

Abstract—Porous $La_{0.6}Sr_{0.4}Co_{0.2}Fe_{0.8}O_{3-\delta}$ ceramic films with different porosities were fabricated by constrained sintering on dense substrates of Gd-doped ceria at 900-1200 °C. The actual digital three dimensional microstructures of the as-sintered films were reconstructed using focused ion beam/scanning electron microscope tomography and their elastic moduli were calculated using finite element modelling based on the reconstructed microstructures. The calculated moduli were found to be in good agreement with experimental results. Porosity was found to be the primary factor influencing the elastic modulus. In order to explore the influence of microstructural features other than porosity the real microstructures, and artificial microstructures based on spherical mono-size particles, were coarsened numerically at constant porosity using a cellular automaton method. The simulation results showed that in the initial stages of sintering, when interparticle necks are small, the modulus increases with the neck size. However, as the coarsening increases further, the modulus becomes insensitive to the details of the microstructure and only depends on porosity. The results also show that simulation gives inaccurate results if the ratio of characteristic length of the simulated volume to the characteristic length of the microstructure is too small (less than approximately a factor of 8).

Keywords: Elastic modulus; Porous solid; FIB/SEM tomography; Microstructure; Finite element modelling

1. Introduction

The elasticity of porous solids has been extensively studied in the past few decades. Focus has been mainly on the description and prediction of the porosity-dependent mechanical properties such as effective strength, elastic modulus and shear modulus, particularly for ceramic materials prepared by partial sintering of powders. The relationships between elastic modulus and microstructure for partially sintered powders are likely to be quite different from those of similar porous material made by other processing methods (e.g., foams and cellular ceramics) [1,2].

A number of equations, either empirical or semi-empirical, have been proposed to relate elastic properties of porous solids to fractional pore volume. These are based either on fitting experimentally measured data or numerical simulations of ideal regular microstructures. Recently a thorough overview was given by Pabst et al. [3] covering most elastic modulus–porosity relations proposed in the literature and examining the theoretical background and merit of the different relationships. Examples of these commonly used expressions include the linear relationship first developed by Fryxell and Chandler [4] for polycrystalline BeO and a simple exponential relationship proposed by Spriggs [5] for fitting the experimentally measured modulus of porous ceramics. Other non-linear expressions include the Coble–Kingery non-linear relation [1] for solids containing isolated pores, the Phani–Niyogi power-law relation [6,7] to better describe the modulus-porosity data of porous solids over a wide range of porosity and a non-linear relation proposed by Hasselman [8] to ensure that the fitted modulus becomes 0 when porosity reaches 100%. However, most of the relations apply only for narrow ranges of porosity, specific materials or special cases, such as porous materials with a dilute distribution of spherical pores. Furthermore these approaches do not explicitly take into account microstructural parameters other than porosity.

The aim of the present study is to explore how elastic modulus of a typical partially sintered ceramic film depends on its microstructure and whether factors other than porosity have significant influence. This is based on both real 3D microstructures of partially sintered films and artificial microstructures formed from an initial random distribution of uniform mono-size spherical particles. In order to examine microstructure parameters other than porosity, the starting microstructures were coarsened by computer simulation at constant porosity using a cellular automaton (CA) method that mimics mass transport by evaporation and condensation. The elastic properties of the original and coarsened microstructures were then computed using a mechanical FEM simulation and correlated with characteristic quantifiable microstructural features.

The perovskite $La_{0.6}Sr_{0.4}Co_{0.2}Fe_{0.8}O_{3-\delta}$ (LSCF) is a common cathode material used in intermediate temperature solid oxide fuel cells (IT-SOFCs) [9,10] due to its

* Corresponding author.

http://dx.doi.org/10.1016/j.actamat.2015.02.014
1359-6462/

stability, electro-catalytic activity for oxygen reduction, and high electronic and ionic conductivity [11,12]. In this work LSCF films were fabricated by slurry casting followed by sintering at different temperatures ranging from 900 to 1200 °C, resulting in porous films having different pore volume fractions and microstructures. Tomography technique (using either X-ray or FIB/SEM) has emerged over the past few decades as one of the powerful tools for quantitative characterisation and analysis of microstructural and functional properties in many-body physics [13,14]. The actual 3D image based modelling was first made possible largely thanks to the X-ray tomography employed [15,16]. Similarly, the latter FIB/SEM tomography technique allows the 3D reconstruction and analysis of the real spatial microstructures of porous electrodes [17] and has been used in the past to relate their microstructure to electrochemical performance [18–21]. The current study uses this approach to correlate microstructure with elastic mechanical properties.

2. Materials and methods

2.1. Specimen preparation and characterisation

Porous LSCF films were produced on dense substrates of $Ce_{0.9}Gd_{0.1}O_{1.95}$ (CGO) by slurry casting and sintering at 900, 1000, 1100 or 1200 °C as described previously [22].

The room temperature film-only elastic moduli were determined for the as-sintered porous LSCF films by nanoindentation using a diamond spherical indenter, based on the Oliver–Pharr method [23], and the details are given in [22].

The surface and cross-sectional microstructures of the specimens were studied in 2D using a scanning electron microscope (JSM-5610LV SEM, JEOL, Japan). For 3D characterisation a focused ion beam/scanning electron microscope (FIB/SEM) dual-beam instrument (Helios NanoLab 600i, FEI, USA) was used for sectioning and imaging sequential 2D cross-sectional surface images of the porous specimens. Before FIB sectioning, the specimens were impregnated with low viscosity epoxy resin under vacuum to enhance the grayscale contrast and edge definition between the pore phase and solid phase, and to ensure that the highly porous structures outside the sectioning region remained intact. The so-called "shine-through" effect could also be avoided by the resin impregnation [24]. The specimen was then coated with a thin layer of gold to provide good electronic conductivity and an additional protective platinum layer of 1–2 μm thickness was then deposited on the top surface of the specimen within the FIB/SEM vacuum chamber in order to protect the upper surface and to prevent charging during sectioning and imaging.

A volume of interest (VOI) $20 \times 15 \times 20$ μm was machined for serial sectioning with a cross-shaped fiducial mark to facilitate automatic image registration. Artefacts caused by tilting, drifting and curtaining were manually corrected or minimised by optimising the working parameters [25]. A resolution of 12.5 nm/pixel was used for SEM imaging and thus a 12.5 nm distance was also applied between sectioning of two consecutive images, so that cubic shape voxels were generated. As a result, several hundred 2D images were obtained for each VOI (e.g., Fig. 1(a)).

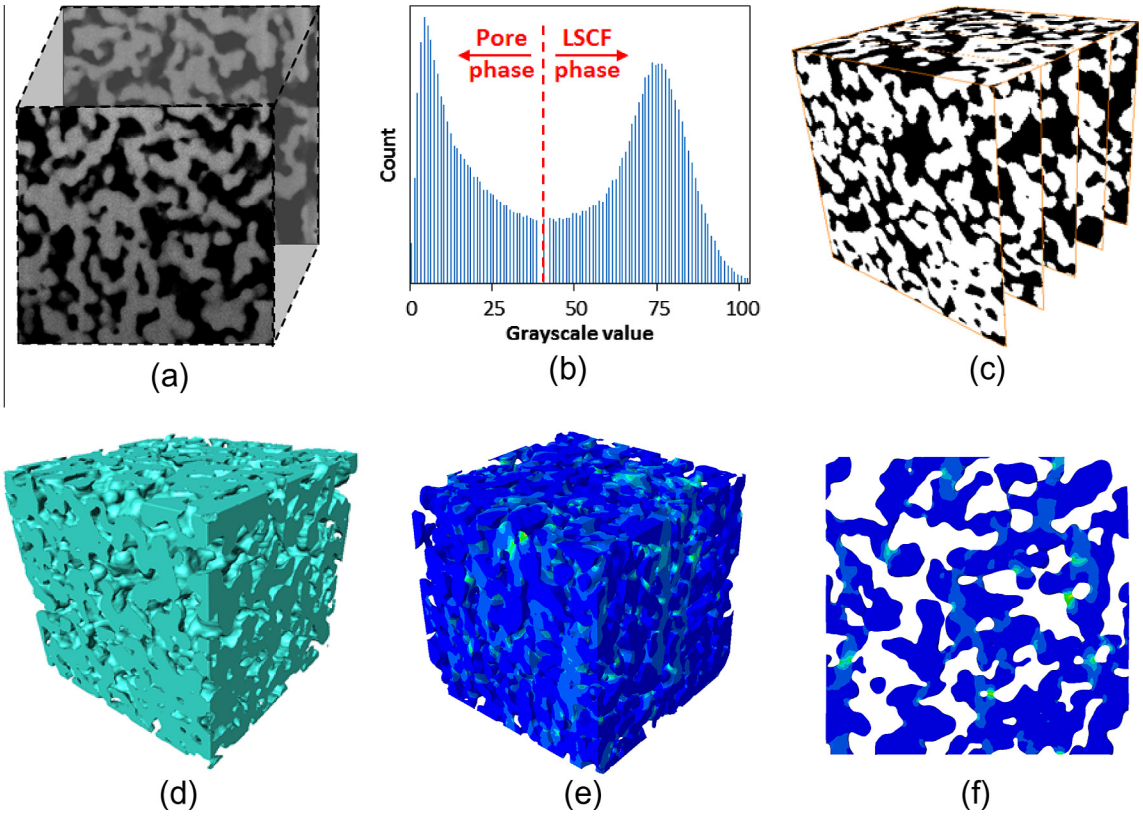

Fig. 1. Segmentation and reconstruction: (a) sequential grayscale images acquired, (b) thresholding segmentation based on grayscale histogram, (c) image stack after segmentation (black = pore, white = solid), (d) the reconstructed 3D microstructure generated, (e) 3D stress contour plot of the actual microstructure using FEM and (f) 2D cross-sectional stress contour plot.

In the current study, at least three VOIs at different locations of each individual specimen were characterised.

Image processing and reconstruction of the 3D microstructure was carried out using Avizo Fire 8.0 3D reconstruction software (VSG Co., USA). The reconstruction process involved: alignment of the image stack; image refinement (removal of noise and gradients); adjustment of image resolution (i.e. downsampling when a dataset was too large); segmentation by grayscale thresholding; and 3D model generation.

The threshold value for binarising the images (i.e. segmentation into pore and solid phases) was set to be the minimum value between the two peaks in the grayscale histogram, as shown in Fig. 1(b). Applying this value to segmentation of the initial images resulted in the binary images shown in Fig. 1(c). The black areas (grayscale value = 0) were assigned as pores and the white as solid (LSCF). Once this was done for each 2D image, the pore space and solid space were interconnected respectively through the third dimension to generate the 3D reconstruction, as shown in Fig. 1(d). In addition, the demonstration of typical simulation-generated stress distribution contours of the actual microstructure in Fig. 1(e and f) is to further show the interest of such advantageous image based computations.

The basic microstructural parameters including 2D planar porosities of serial images and 3D volumetric porosities of microstructures were determined using Avizo's quantification module. The tortuosity of each phase was computed using Avizo's *Centroid Path Tortuosity* module and the particle/pore size and neck/aperture size distributions were quantified using Avizo's "Separate Objects" module [26] based on watershed, distance transform and numerical reconstruction algorithms [27,28].

After a solid/porous phase was separated into a group of individual particles (or pores), the volume of each particle/pore was converted to an Equivalent Spherical Diameter (ESD) for plotting particle/pore size distribution histograms. Similarly, the surface area of a neck was converted into an Equivalent Circular Diameter (ECD) for neck size distribution analysis [29]. Note that the amount of neck surface area was determined by the resulting triangulated surfaces, which significantly increased the accuracy of measurement compared to the use of pixelised surfaces.

2.2. Finite element modelling

For computational convenience, a smaller volume in the range of 3^3–12^3 μm^3, consisting of 240–960 serial 2D images, was extracted from the initial VOI for mechanical modelling. This resulted in a 3D microstructural dataset with voxel size 12.5^3 nm^3. The 3D reconstructed microstructure was then processed using ScanIP 6.9 software (Simpleware, UK) to generate tetrahedral meshes for the solid phase, to be used in the FEM simulation. The ScanIP module + FE Free meshing algorithm was used which allowed adaptive mesh generation with varying mesh element size depending on the microstructural feature size. This generated at least 6 million tetrahedral elements for each microstructure. The generation of such a large number of elements took up to 3 h to finish on a workstation configured with Intel Xeon 12-core 2.76 GHz processor and 96 GB RAM.

After mesh generation, the 3D microstructures were exported as FE compatible models into Abaqus CAE 6.12 (Dassault Systemes, USA) for computing their effective elastic moduli. The values of Young's modulus and Poisson's ratio for the dense solid were $E_0 = 175$ GPa and $\nu_s = 0.31$ [30]. The simulation used the Abaqus Standard FE solver based on the assumption that the solid was isotropic and linear elastic. The major axes of the simulation are denoted X and Z, in the film plane, and Y normal to the film plane. The boundary conditions applied are summarised in Table 1. Each of the models was subjected to three simulation tests (denoted Test 1, 2 and 3) to calculate the elastic modulus along the three major axes (X, Y and Z). The boundary condition *U1* means displacement along the X axis, *U2* along the Y axis, and *U3* along the Z axis. The negative displacements correspond to compression.

Boundary conditions were also applied to constrain the degree of freedom of the normal displacements for the nodes on the model's other surfaces parallel to the forced displacement so that these surfaces could contract or expand freely once the forced displacement was applied.

The resultant total normal reaction force on the displaced surface was obtained from the simulation so that the effective elastic modulus (*E2*) of the 3D microstructure could be determined using the total surface area of the displaced surface of the VOI to calculate the average applied stress. Each elastic modulus computing process generally completed within only 30 min due to the FEM involving only single phase models for simple and small linear elastic deformation. The accumulative time spent in processing, meshing and modelling the datasets could be relatively noticeable. However, it should be emphasised that only by doing so can the structure anisotropy as well the effect on elastic modulus of other factors (such as neck size) be evident.

3. Results and discussion

3.1. Quantification of microstructural parameters

The reconstructed 3D microstructures are shown in Fig. 2(a–d) in the order of increasing sintering temperature from 900 to 1200 °C. From these reconstructed microstructures, the gradual densification due to the increasing sintering temperature can be readily observed.

The corresponding volume fractions and tortuosities of the solid and pore phases are shown in Fig. 3.

As expected, with increasing sintering temperature the total porosity decreased from 46.9 ± 2.2% to 15.2 ± 1.2%. Similar tortuosities were found for both solid and pore

Table 1. Boundary conditions and displacements applied for each model in FEM.

Test no.	Axis	Boundary conditions applied	Displacement applied (Pixel)
1	X	Xmin: $U1 = 0$; Ymin: $U2 = 0$; Zmin: $U3 = 0$	Xmax: $U1 = -1$
2	Y	Xmin: $U1 = 0$; Ymin: $U2 = 0$; Zmin: $U3 = 0$	Ymax: $U2 = -1$
3	Z	Xmin: $U1 = 0$; Ymin: $U2 = 0$; Zmin: $U3 = 0$	Zmax: $U3 = -1$

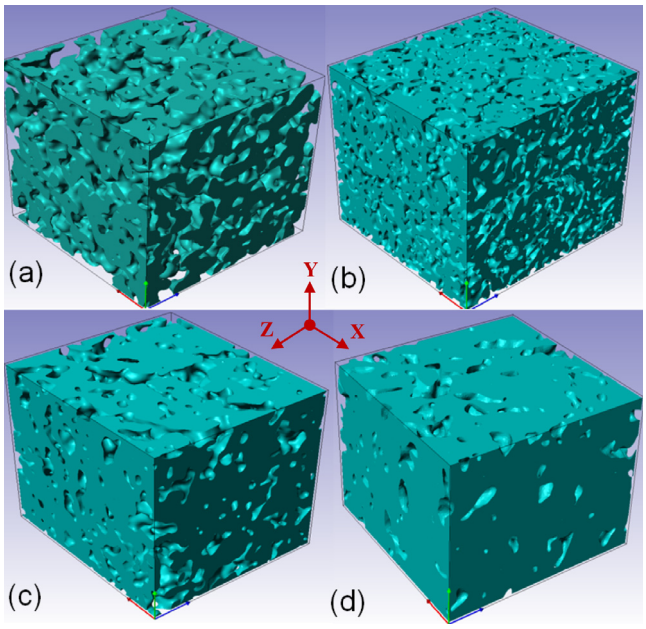

Fig. 2. Examples of the reconstructed 3D microstructures of the 900–1200 °C as-sintered LSCF films, with solid being LSCF and voids being pores.

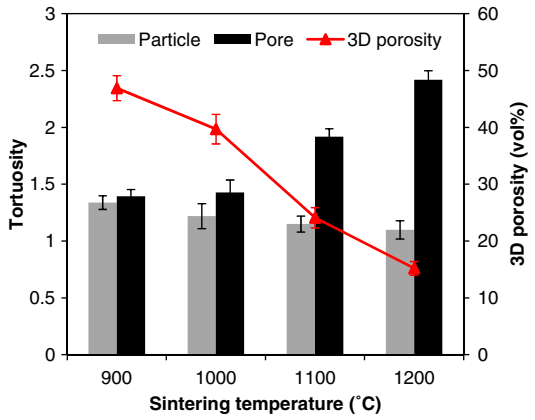

Fig. 3. Comparison of 3D porosities and tortuosities for solid and pore phases in films sintered at different temperatures.

phases in the specimen sintered at 900 °C, with a value of approximately 1.4. This similarity was expected as the porosity was close to 50%. As the porosity reduced, the tortuosity of the pore phase significantly increased, reflecting much more tortuous pore connectivity in the films after sintering at higher temperatures. On the other hand, the tortuosity of the solid phase decreased and approached unity as the density increased.

The mean values and standard deviations of the number distributions of particle size (equivalent spherical diameter, ESD) and inter-particle neck size (equivalent circular diameter, ECD) of the separated solid particles for each sintering temperature are summarised in Table 2.

Table 2. Particle size (ESD) and neck size (ECD) distribution parameters.

Sintering temperature (°C)	ESD (nm)	ECD (nm)
900	470 ± 180	123 ± 66
1000	850 ± 290	191 ± 101
1100	1280 ± 430	440 ± 245
1200	1700 ± 630	706 ± 418

As expected, there is a gradual increase of both particle size and neck size with increasing sintering temperature.

3.2. FEM of elastic modulus

3.2.1. Comparison of FEM-derived elastic moduli with nanoindentation measurements

The elastic modulus derived from FEM for each specimen is compared in Fig. 4 with that measured previously by nanoindentation [22].

The average elastic modulus calculated from the microstructures is found to increase threefold from 28 ± 7 GPa for a sintering temperature of 900 °C to 117 ± 7 GPa for the specimen sintered at 1200 °C. It is also clear from Fig. 4 that for all the samples that the elastic modulus normal to the film plane (*Y* axis) was larger than those in the film plane (*X* and *Z* axes). This type of anisotropy is expected from the constrained sintering of the film, which induces a tensile stress in the film plane during sintering and consequent anisotropy in the microstructure [31].

The anisotropy in the elastic modulus was quantified by calculating the degree of anisotropy, $DA = 1-(E1 + E3)/(2 \times E2)$, now that *E2* was always larger than *E1* and *E3* in the study. Thus DA = 0 corresponds to fully isotropic, and DA = 1, fully anisotropic. It is found that the DA decreased from approximately 0.47–0.11 as the sintering temperature increased from 900 to 1200 °C (i.e. became more isotropic). Despite the complication of anisotropy, the elastic modulus measured by nanoindentation for each sintering temperature was in good agreement with that calculated from the microstructure, and averaged over the three principal directions, to within experimental error.

3.2.2. Dependence of elastic modulus on porosity

Fig. 5 plots the relationship of the elastic moduli obtained by both FEM and nanoindentation with the

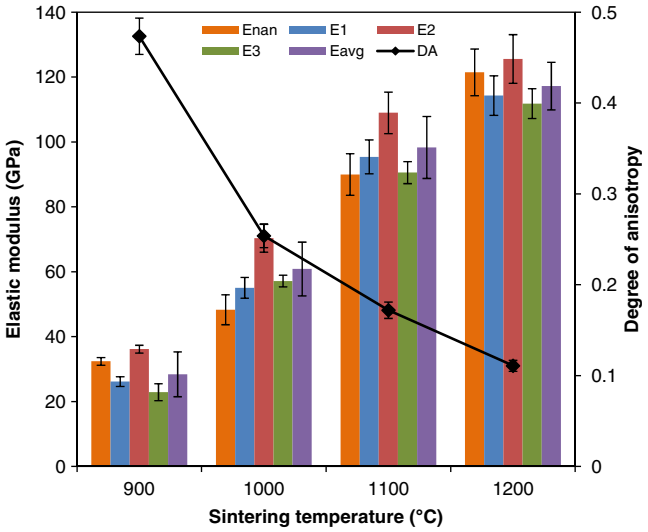

Fig. 4. Comparison of elastic moduli measured by nanoindentation (*Enan*) and calculated by FEM. *E1* is the FEM modulus in the *X* direction, *E2* in *Y* and *E3* in *Z*. *Eavg* is the averaged value of *E1*, *E2* and *E3*. The degree of anisotropy (DA) for each type of microstructure is also plotted.

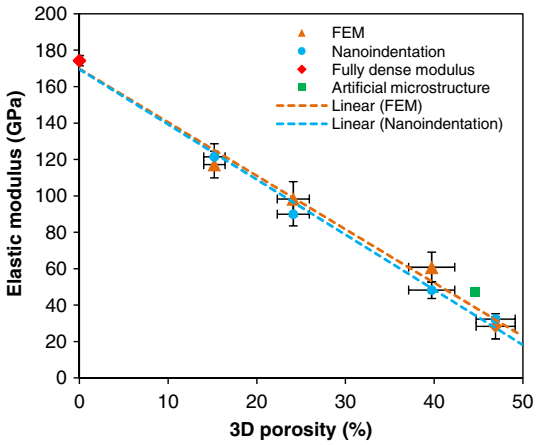

Fig. 5. Elastic moduli derived from FEM and nanoindentation as a function of porosity. The shaded areas are the corresponding standard deviation areas expected.

porosity of the corresponding microstructure. The dotted lines in the figure correspond to linear fits. Note that the previously measured nanoindentation result for the zero porosity bulk sample is also plotted. In addition, the modelled elastic modulus of an artificial microstructure with approximately 44.6% porosity as described later is shown to fall well in the expected range. This will be further discussed in the later section.

3.3. Numerical microstructure modification at constant porosity and influence on elastic modulus

3.3.1. Numerical microstructural modification

In order to investigate how parameters other than porosity would influence the elastic modulus of the porous microstructures, a cellular automaton (CA) algorithm method [32] was used to coarsen the original 3D microstructures. This simulation corresponds to material transport by evaporation/condensation and so does not lead to densification (maintains constant porosity). In the coarsening simulation the microstructure evolved in a sequence of "time steps". In the present simulation these have no physical meaning, but in principle are related to the rate of evaporation of the solid material. An example of the morphological changes induced by the coarsening simulation applied to the microstructure of the film sintered at 1000 °C is shown in 2D in Fig. 6. The microstructural parameters and elastic moduli of the modified microstructures were then computed.

Tortuosity for all the original and modified microstructures including particles and pores were computed and are summarised in Fig. 7(a). The plot reveals that the microstructure evolution had little effect on tortuosity of either the solid or the pores.

The mean and standard deviation for the distributions of ESD of the computationally separated particles and pores in the modified microstructures are compared with the original ones in Fig. 7(b). The results show that the pores and particles both increase in size as expected. It should be noted that the large error bars do not represent errors but correspond to the standard deviations as a result of size distribution measurements.

The mean and standard deviation for the distributions of ECD for inter-particle necks of the computationally separated particles in the modified microstructures are compared with the original ones in Fig. 7(c). The results show that the necks increase in size as expected.

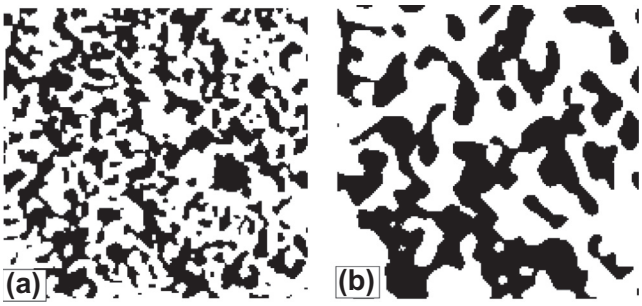

Fig. 6. Microstructure evolution simulated by the coarsening algorithm applied to the microstructure of the film sintered at 1000 °C after (a) 0 and (b) 20 time steps. White pixels represent solid and black pore phase.

3.3.2. Effect of coarsening on elastic modulus of the film microstructures

After microstructure modification for different numbers of time steps (i.e. 2, 5, 10 and 20) using the CA based method, the elastic modulus of the coarsened microstructures was calculated by FEM. To facilitate comparison, the computed elastic moduli for each time step were averaged over the values for the three principal directions and then normalised relative to the average value for the original microstructure. The results are plotted in Fig. 8.

Hardy and Green [33] studied the elastic modulus of partially sintered alumina and found significant increase in elastic modulus with even minimal densification which they ascribed to neck growth by surface diffusion. However, the simulations in the current study display a different behaviour in that in only one case does the modulus increase with neck size and in one case there is a marked reduction in modulus. In order to understand this, similar coarsening simulations were carried out on artificial microstructures formed from initially spherical particles. As far as we were aware of, the CA algorithm did not generate any bias in the porosity and surface area to volume ratio of the microstructures in the course of modification. As will be returned to in further details in the later discussion, the difference of increase and decrease in modulus is a result of the critical volume size being satisfied or not after coarsening (here only the 900 °C sample does). The much larger drop in modulus for the 1000 °C sample is due to the relatively greater change in microstructure compared with the ones for 1100 °C and 1200 °C after coarsening, as the initial microstructures of the latter two already possess larger particles and thus the coarsening generates smaller relative changes in the microstructures, as also suggested by Fig. 7(b and c).

3.4. Modulus and coarsening of artificial microstructures

In the light of work done by Rhazaoui et al. [34], the starting artificial microstructure was generated by randomly packing a cube of a volume size = 200^3 voxel (i.e. pixel^3) with two types of mono-size spheres (diameter = 20 pixel and 10 pixel, respectively) representing the solid and pore phases. Once the cube was densely packed with spheres in tangent contact, the spheres representing pores were

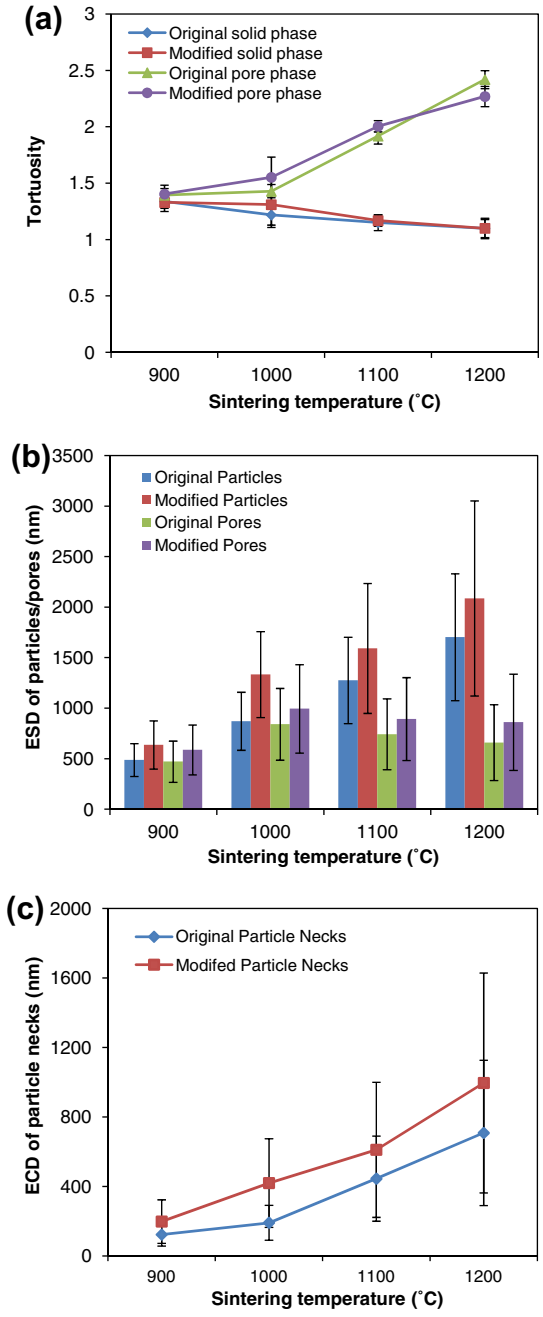

Fig. 7. Comparison of microstructural parameters before and after microstructural modification for 20 time steps, (a) tortuosity factors, (b) ESD of separated particles and pores and (c) ECD of the necks between separated particles.

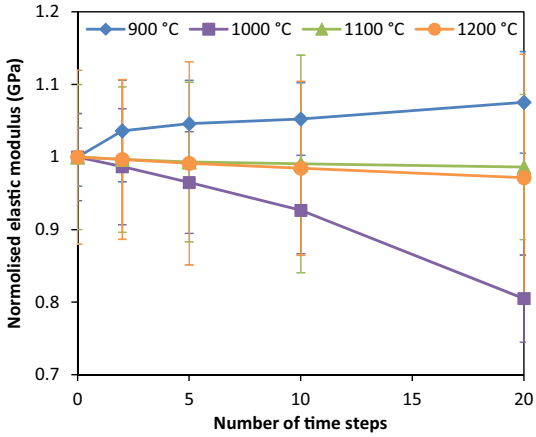

Fig. 8. Comparison of the averaged normalised elastic moduli estimated by FEM for original and modified microstructures.

removed and, together with the unfilled regions, the total voids in the cube now represented the real pore phase. This resulted in a total porosity of ~44.6% in the cubic microstructure. As with the real microstructures, the starting artificial microstructure was coarsened using the CA algorithm while the porosity was kept constant. In this way, a series of modified microstructures was successively generated after different numbers of time steps (2, 4, 20, 40, 70, 100 and 200).

Fig. 9 shows examples of the 2D cross-sectional images of the same plane as the microstructure evolved (in which white represents solid and black pores) and the corresponding 3D representations.

The images in Fig. 9(b and c) show that at short times (2 and 4 time steps) the necks between the particles are formed and the original particles are still discernable. However, after further coarsening the identity of the original particles is lost and an overall interconnected solid network has formed. In the later stages, coarsening "magnifies" the network in what appears to be a self-similar manner (i.e. the microstructures after 70 time steps and above appear to differ only in magnification).

By using the same methods of 3D reconstruction and FEM as for the LSCF microstructures, the elastic modulus of each modified microstructure in the three principal directions was estimated, and the results are presented in Fig. 10.

In principle the elastic modulus of these artificial microstructures should be isotropic. The results in Fig. 10 show that this is the case after short coarsening times, but a small anisotropy appears to develop as the coarsening increases. This is an artefact of the scale of the microstructure compared with the scale of the VOI and will be returned to in the later discussion.

Fig. 10 shows that as a result of coarsening the elastic modulus first increased significantly until the number of time steps reached approximately 40, after which a gradual fall took place. Comparison with the evolving microstructures in Fig. 9 shows that the initial increase is due to the growth of necks at the particle contacts which increases the size of the load-transmission areas between particles. Once the identification of particles in the microstructure is no longer possible, the concept of load transmission at necks between particles becomes meaningless.

The fall in modulus for time steps >40 is unexpected and therefore it was considered necessary to examine the influence of sampling in the calculation of the elastic modulus. In particular, a sufficiently large volume must be simulated in order to be statistically representative of the porous material [35]. Such a volume is known as a representative volume element (RVE) [36]. Any modelled volume larger than the critical minimum RVE can be regarded representative. However, a small RVE is desirable from the point of view of computational efficiency and therefore in practice a compromise is necessary.

The determination of the minimum RVE size of a non-uniform microstructure containing randomly distributed particles has been extensively studied in the past years, using various statistical-numerical analyses [35–41]. The

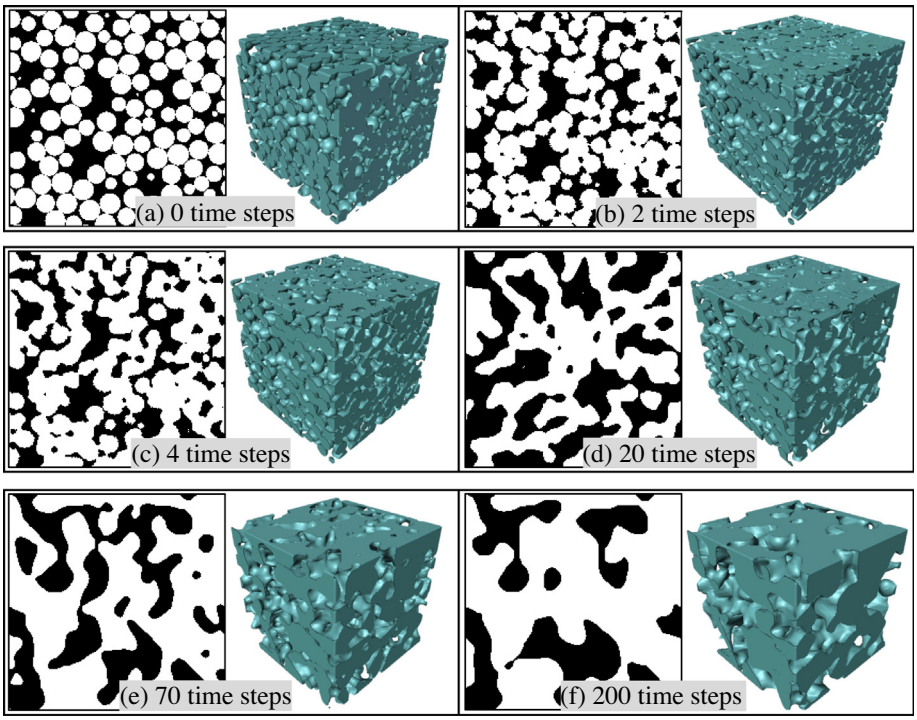

Fig. 9. 2D and 3D representations of the artificial microstructures after different degrees of coarsening.

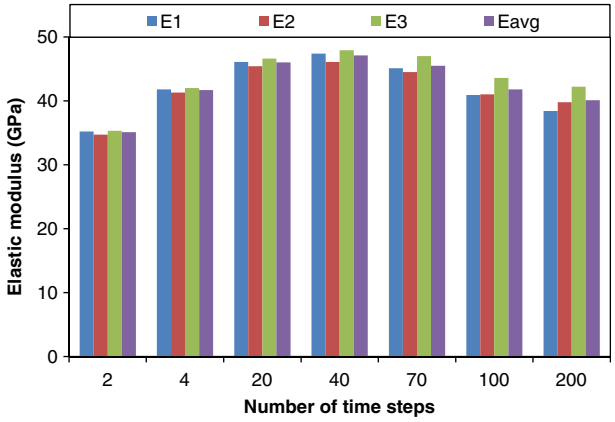

Fig. 10. Computed elastic moduli in the three principal directions and the average value for the artificial microstructures coarsened for varying time steps.

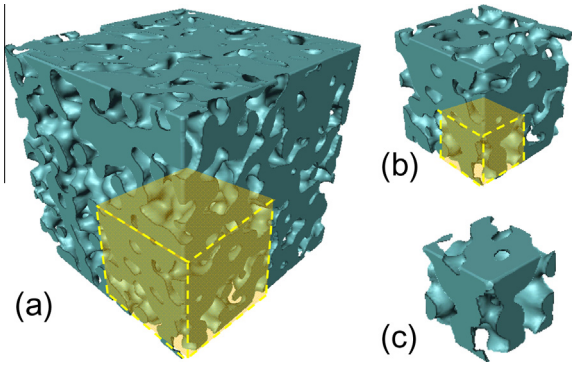

Fig. 11. Examples of the two partitioning procedures to generate smaller volumes for calculating the elastic modulus of the artificial microstructure coarsened for 20 time steps (a) volume size = 200^3 -pixel^3, (b) 100^3 pixel^3, and (c) 50^3 pixel^3. Transparent boxes mark the partitioning of smaller volumes from larger volumes.

general approach is to link the size of the RVE to the size of critical features, such as particles, in order that the effective macroscopic property under consideration is estimated to within a given precision (usually a relative error ~5%). For example, Van Mier [41] reported the critical RVE linear size to be approximately 7–8 times the largest inclusion or particle size for estimating the properties of concrete. For a volume larger than the minimum RVE size, the overall property computed would be insensitive to the volume size, the sampling location and the number of samples [39].

In order to examine this in the present study the artificial microstructure coarsened for 20 time steps was selected and being typical of having a large volumetric cube side (L) of 200 pixel and particle size (D) of 20 pixel. The coarsened microstructure was partitioned into a set of 8 equal size cubes with $L = 100$ pixel and a set of 64 cubes with $L = 50$ pixel as shown in Fig. 11.

The results are summarised in Table 3 in terms of mean values and ±one standard deviation for the smaller volume sets. Only 11 of the 64 smallest volumes were analysed to save computational time. The results show that as the RVE decreases, the standard deviations of both the porosity and the elastic modulus increase. This is to be expected as the statistically varying relative differences between the individual volumes are larger as the volumes become smaller. However, the smaller volumes also introduced a bias in the mean values such that the porosity appeared larger and the elastic modulus smaller as volume decreased. The bias in the mean value of the computed modulus is suggested to be caused by larger relative heterogeneity in the smaller volumes as reflected in the increased standard deviation. The more heterogeneous the microstructure, the greater is the effect of the more compliant parts of the structure which

Table 3. Averaged estimation of 3D porosity and elastic modulus for different sets of volume.

Volume size (pixel^3)	Porosity (vol.%)	Elastic modulus (GPa)
50^3	46.8 ± 6.3	40.5 ± 11.6
100^3	44.6 ± 1.4	43.9 ± 2.6
200^3	44.6	46

results in a lower apparent modulus. For the volume of 100^3 pixel^3 the relative error in the mean of the modulus, compared with the result for the full volume, is 2.1/46 or 4.6% which suggests that the critical L/D ratio is greater than 5. The reason for the bias in the mean value of porosity of the smallest volume is attributed to the limited sample number.

It is therefore likely that the reduction in computed elastic modulus for the coarsened real and artificial microstructures observed at the higher levels of coarsening is an artefact caused by the volume being much smaller than the minimum RVE required for the coarser microstructures. The results in Fig. 10 show that the reduction in computed modulus becomes evident for coarsening beyond 40 time steps for which $L/D = 200/25.7 = 7.8$. This value is close to other reported values for the critical L/D in the literature. Cai et al. [42] suggested a critical L/D of 7.5 for fuel cell anode microstructures of 21.5% porosity and a critical value of 7 was reported by Joos et al. [43] for cathode microstructures containing 30–50% porosity. In conclusion, the results from the analysis of the coarsened artificial microstructures indicate that when the original particles are still identifiable in the microstructure, the elastic modulus increases as the relative neck size to particle size increases. However, once the original particles are no longer discernable the modulus is relatively insensitive to the details of the microstructure and depends only on porosity. For the coarsening model used in this study, the microstructures eventually become self-similar and differ only in scale.

To assess this effect of RVE on the coarsened microstructures of the LSCF films, the ratio of L/D was calculated for each case and the results are plotted in Fig. 12 along with the minimum L/D ratio (shown as a horizontal red line) required for a volume to be representative.

The results show that only in the case of the film sintered at 900 °C can the original and coarsened microstructures be considered to have been analysed at an appropriate RVE. The other as-sintered microstructures are close to the critical RVE, but as they are coarsened the volumes become too small to be truly representative. Thus the observed reduction in modulus with coarsening is most likely an artefact of the volumes becoming progressively smaller than the critical RVE value.

Returning to the results of the simulations using the artificial microstructures, in the light of the discussion above, the modulus for the microstructure after coarsening for 40 time steps gives the best estimate for a well-developed typical microstructure and, for LSCF gives a modulus of 47 GPa at a porosity of 45%. This is shown plotted in Fig. 5 together with the experimental results with which it is in good agreement. This supports the general conclusion that in porous ceramics made from partially sintered powder particles porosity is the key variable and detailed features of the microstructure have only minor influence.

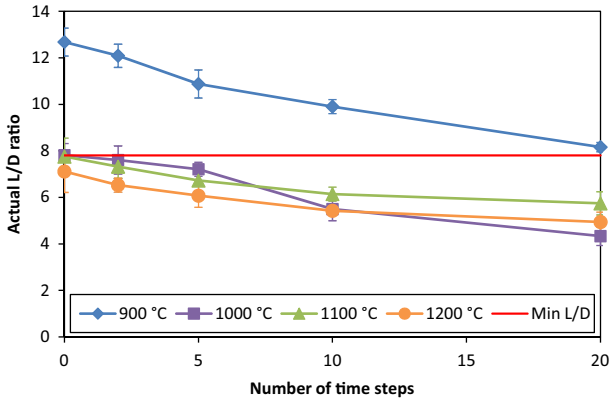

Fig. 12. Comparison of the actual L/D ratios for all sets of microstructures and the previously derived Minimum ratio (Min $L/D = 7.8$, shown as a red line). (For interpretation of the references to colour in this figure legend, the reader is referred to the web version of this article.)

4. Conclusions

The elastic moduli of the porous LSCF films produced in this study were reliably calculated using FEM based on the 3D microstructures reconstructed using FIB/SEM tomography. The computed moduli were in good agreement with experimental values previously measured by nanoindentation of the same films. The calculated moduli perpendicular to the film plane was up to approximately 40% larger than the modulus in the film plane. This is a consequence of anisotropy in the microstructure which is caused by constrained sintering of the films. The anisotropy decreased to approximately 10% as both the porosity and pore size decreased.

The main microstructure parameter influencing elastic modulus is porosity. Simulations with artificial microstructures sintering with an evaporation/condensation process, showed that in the early stages of sintering (at constant porosity) neck growth between particles had a significant effect on the modulus which increased by approximately 30% during this initial period. However, once microstructure became "mature" (i.e. when the initial particles could no longer be identified) further coarsening resulted in self-similar microstructures with no change in modulus. Coarsening simulations of the real film microstructures showed that only the film with the lowest density did not have a "mature" microstructure. For this film the coarsening simulations showed a modest increase in modulus of less than 10% due to continuing neck growth. All the other films showed an apparent decrease in modulus with simulated coarsening. This is caused by a sampling artefact and it is likely that the un-coarsened microstructures of these films were already "mature" and that the coarsening gave self-similar microstructures with constant modulus.

It was found that there existed a critical minimum ratio of the linear dimension of the representative volume element (RVE) L, and the "particle" diameter (or characteristic feature size) of the microstructure D, for determining a statistically representative elastic modulus (to within 5% of the true value) by FEM simulation. Below this critical value of 8, the heterogeneity of the porous microstructure leads to FEM underestimating the true modulus.

The modulus calculated for a "mature" microstructure formed from an initial assembly of mono-size spherical particles was in good agreement with the experimentally measured modulus and that calculated by FEM from the real microstructure of a film of the same porosity. This confirms that for porous ceramics made from partially sintered powder particles, porosity is the key variable that controls elastic modulus and that other features of the microstructure have only minor influence.

Acknowledgements

This research was carried out as part of the UK Supergen consortium project on "Fuel Cells: Powering a Greener Future". The Energy Programme is an RCUK cross-council initiative led by EPSRC and contributed to by ESRC, NERC, BBSRC and STFC. Dr. Chen is especially grateful to the Chinese Government and Imperial College for financial support in the form of scholarships. Thanks are additionally due to Dr. Rhazaoui for help in generating the original artificial microstructure, Dr. Farid Tariq and Prof. Nigel Brandon for assistance with simulation.

References

[1] R. Coble, W. Kingery, Effect of porosity on physical properties of sintered alumina, J. Am. Ceram. Soc. 39 (1956) 377–385.
[2] E.A. Dean, J.A. Lopez, Empirical dependence of elastic moduli on porosity for ceramic materials, J. Am. Ceram. Soc. 66 (1983) 366–370.
[3] W. Pabst, E. Gregorová, G. Tichá, Elasticity of porous ceramics—a critical study of modulus–porosity relations, J. Eur. Ceram. Soc. 26 (2006) 1085–1097.
[4] R. Fryxell, B. Chandler, Creep, strength, expansion, and elastic moduli of sintered BeO as a function of grain size, porosity, and grain orientation, J. Eur. Ceram. Soc. 47 (1964) 283–291.
[5] R. Spriggs, Expression for effect of porosity on elastic modulus of polycrystalline refractory materials, particularly aluminum oxide, J. Eur. Ceram. Soc. 44 (1961) 628–629.
[6] K.K. Phani, S.K. Niyogi, Elastic modulus–porosity relation in polycrystalline rare-earth oxides, J. Am. Ceram. Soc. 70 (1987) C-362–C-366.
[7] K. Phani, S. Niyogi, Young's modulus of porous brittle solids, J. Mater. Sci. 22 (1987) 257–263.
[8] D. Hasselman, On the porosity dependence of the elastic moduli of polycrystalline refractory materials, J. Am. Ceram. Soc. 45 (1962) 452–453.
[9] D. Waller, J. Lane, J. Kilner, B. Steele, The effect of thermal treatment on the resistance of LSCF electrodes on gadolinia doped ceria electrolytes, Solid State Ionics 86 (1996) 767–772.
[10] L.-W. Tai, Structure and electrical properties of La1-xSrxCo1-yFeyO3. Part 1. The system La0.8Sr0.2Co1-yFeyO3, Solid State Ionics 76 (1995) 259–271.
[11] L.W. Tai, M.M. Nasrallah, H.U. Anderson, D.M. Sparlin, S.R. Sehlin, Structure and electrical properties of La1-xSrxCo1-yFeyO3. Part 2. The system La1-xSrxCo0.2-Fe0.8O3, Solid State Ionics (1995) 273–283.
[12] J.W. Stevenson, T.R. Armstrong, R.D. Carneim, L.R. Pederson, W.J. Weber, Electrochemical properties of mixed conducting perovskites La1-xMxCo1-yFeyO3-δ (M = Sr, Ba, Ca), J. Electrochem. Soc. 143 (1996) 2722–2729.
[13] L. Holzer, M. Cantoni. Review of FIB-tomography, Nanofabrication Using Focused Ion and Electron Beams: Principles and Applications 2011 (2011).
[14] E. Maire, P. Withers, Quantitative X-ray tomography, Int. Mater. Rev. 59 (2014) 1–43.
[15] D. Ulrich, B. van Rietbergen, H. Weinans, P. Rüegsegger, Finite element analysis of trabecular bone structure: a comparison of image-based meshing techniques, J. Biomech. 31 (1998) 1187–1192.
[16] E. Maire, A. Fazekas, L. Salvo, R. Dendievel, S. Youssef, P. Cloetens, J.M. Letang, X-ray tomography applied to the characterization of cellular materials. Related finite element modeling problems, Compos. Sci. Technol. 63 (2003) 2431–2443.
[17] J.R. Wilson, W. Kobsiriphat, R. Mendoza, H.-Y. Chen, J.M. Hiller, D.J. Miller, K. Thornton, P.W. Voorhees, S.B. Adler, S.A. Barnett, Three-dimensional reconstruction of a solid-oxide fuel-cell anode, Nat. Mater. 5 (2006) 541–544.
[18] D. Gostovic, J.R. Smith, D.P. Kundinger, K.S. Jones, E.D. Wachsman, Three-dimensional reconstruction of porous LSCF cathodes, Electrochem. Solid-State Lett. 10 (2007) B214.
[19] J. Joos, T. Carraro, A. Weber, E. Ivers-Tiffée, Reconstruction of porous electrodes by FIB/SEM for detailed microstructure modeling, J. Power Sources (2010).
[20] K. Matsuzaki, N. Shikazono, N. Kasagi, Three-dimensional numerical analysis of mixed ionic and electronic conducting cathode reconstructed by focused ion beam scanning electron microscope, J. Power Sources 196 (2011) 3073–3082.
[21] D. Marinha, L. Dessemond, J.S. Cronin, J.R. Wilson, S.A. Barnett, E. Djurado, Microstructural 3D reconstruction and performance evaluation of LSCF cathodes obtained by electrostatic spray deposition, Chem. Mater. 23 (2011) 5340–5348.
[22] Z. Chen, X. Wang, V. Bhakhri, F. Giuliani, A. Atkinson, Nanoindentation of porous bulk and thin films of La0.6Sr0.4Co0.2Fe0.8O3−δ, Acta Mater. 61 (2013) 5720–5734.
[23] W.C. Oliver, G.M. Pharr, An improved technique for determining hardness and elastic modulus using load and displacement sensing indentation experiments, J. Mater. Res. 7 (1992) 1564–1583.
[24] T. Prill, K. Schladitz, D. Jeulin, M. Faessel, C. Wieser, Morphological segmentation of FIB-SEM data of highly porous media, J. Microsc. 250 (2013) 77–87.
[25] L.A. Giannuzzi, Introduction to focused ion beams: instrumentation, theory, techniques and practice, Springer, 2004.
[26] Avizo User Guide. Visualization Sciences Group, SAS, 2013.
[27] A.P. Mangan, R.T. Whitaker, Partitioning 3D surface meshes using watershed segmentation, visualization and computer graphics, IEEE Trans. 5 (1999) 308–321.
[28] R. Atwood, J. Jones, P. Lee, L. Hench, Analysis of pore interconnectivity in bioactive glass foams using X-ray microtomography, Scripta Mater. 51 (2004) 1029–1033.
[29] Z. Chen. Mechanical Properties of La0.6Sr0.4Co0.2Fe0.8O3-d Fuel Cell Electrodes. vol. PhD: Imperial College London, 2014.
[30] Y.-S. Chou, J.W. Stevenson, T.R. TArmstrong, L.R. LPederson, Mechanical properties of La1-xSrxCo0.2Fe0.8O3-ä mixed-conducting perovskites made by the combustion synthesis technique, J. Am. Ceram. Soc. 83 (2000) 1457–1464.
[31] X. Wang, A. Atkinson, Microstructure evolution in thin zirconia films: experimental observation and modelling, Acta Mater. 59 (2011) 2514–2525.
[32] X. Wang, A. Atkinson, Cellular automata modelling of microstructure evolution of Ni cermet anode, ECS Trans. 57 (2013) 2465–2473.
[33] D. Hardy, D.J. Green, Mechanical properties of a partially sintered alumina, J. Eur. Ceram. Soc. 15 (1995) 769–775.
[34] K. Rhazaoui, SOFC microstructure and performance modeling, Earth Science and Engineering, Imperial College London, London, UK, 2014, vol. Ph.D.
[35] T. Kanit, S. Forest, I. Galliet, V. Mounoury, D. Jeulin, Determination of the size of the representative volume element for random composites: statistical and numerical approach, Int. J. Solids Struct. 40 (2003) 3647–3679.
[36] C. Pelissou, J. Baccou, Y. Monerie, F. Perales, Determination of the size of the representative volume element for random quasi-brittle composites, Int. J. Solids Struct. 46 (2009) 2842–2855.

[37] S. Kari, H. Berger, R. Rodriguez-Ramos, U. Gabbert, Computational evaluation of effective material properties of composites reinforced by randomly distributed spherical particles, Compos. Struct. 77 (2007) 223–231.
[38] I. Gitman, H. Askes, L. Sluys, Representative volume: existence and size determination, Eng. Fract. Mech. 74 (2007) 2518–2534.
[39] M. Ostoja-Starzewski, Material spatial randomness: from statistical to representative volume element, Probab. Eng. Mech. 21 (2006) 112–132.
[40] W. Drugan, J. Willis, A micromechanics-based nonlocal constitutive equation and estimates of representative volume element size for elastic composites, J. Mech. Phys. Solids 44 (1996) 497–524.
[41] J.G. van Mier. Microstructural effects on fracture scaling in concrete, rock and ice. IUTAM symposium on scaling laws in ice mechanics and ice dynamics: Springer, 2001. p.171-182.
[42] Q. Cai, C.S. Adjiman, N.P. Brandon, Modelling the 3D microstructure and performance of solid oxide fuel cell electrodes: computational parameters, Electrochim. Acta 56 (2011) 5804–5814.
[43] J. Joos, M. Ender, T. Carraro, A. Weber, E. Ivers-Tiffée, Representative volume element size for accurate solid oxide fuel cell cathode reconstructions from focused ion beam tomography data, Electrochim. Acta 82 (2012) 268–276.